Mon. Not. R. Astron. Soc. **000**, 000–000 (0000)   Printed 29 September 2009   (MN LaTeX style file v2.2)

arXiv:0909.5333v1 [astro-ph.CO] 29 Sep 2009

Self-gravitating warped discs around supermassive black holes

A. Ulubay-Siddiki[1]*, O. Gerhard[1], and M. Arnaboldi[2]
[1] *Max-Planck-Institut für Extraterrestrische Physik, Giessenbachstraße, D-85748 Garching, Germany*
[2] *ESO, Karl-Schwarzschild-Str. 2, D-85748 Garching, Germany*

29 September 2009

ABSTRACT

We consider warped equilibrium configurations for stellar and gaseous disks in the Keplerian force-field of a supermassive black hole, assuming that the self-gravity of the disk provides the only acting torques. Modeling the disk as a collection of concentric circular rings, and computing the torques in the non-linear regime, we show that stable, strongly warped precessing equilibria are possible. These solutions exist for a wide range of disk-to-black hole mass ratios M_d/M_{bh}, can span large warp angles of up to $\pm \sim 120\,$deg, have inner and outer boundaries, and extend over a radial range of a factor of typically two to four. These equilibrium configurations obey a scaling relation such that in good approximation $\dot{\phi}/\Omega \propto M_d/M_{bh}$ where $\dot{\phi}$ is the (retrograde) precession frequency and Ω is a characteristic orbital frequency in the disk. Stability was determined using linear perturbation theory and, in a few cases, confirmed by numerical integration of the equations of motion. Most of the precessing equilibria are found to be stable, but some are unstable. The main result of this study is that highly warped disks near black holes can persist for long times without any persistent forcing other than by their self-gravity. The possible relevance of this to galactic nuclei is briefly discussed.

Key words: galaxies: nuclei, Galaxy: centre, stellar dynamics, galaxies: active, galaxies: Seyfert

1 INTRODUCTION

The increasing power and spatial resolution of modern observations has provided evidence that warps are not unique to galactic disks, but appear also on much smaller scales. These include nuclear and accretion disks surrounding supermassive black holes in galactic nuclei (nuclear disks hereafter). The pioneering example is the maser disk of NGC4258. The high velocity masers mapped by Miyoshi et al. (1995) are best explained by the existence of a mildly warped disk extending from 0.13 to 0.26 pc (Herrnstein et al. 1996). The nearby Seyfert galaxies NGC1068 and Circinus also harbor warped disks in their centers (Greenhill et al. 2003a; Gallimore et al. 2004), again traced by the maser emission. Of the ~ 100 massive young stars in the center of our Galaxy about half form a well-defined, warped disk, and some of the others are on a counterrotating structure which may be a dissolving disk (Genzel et al. 2003; Paumard et al. 2006; Lu et al. 2009; Bartko et al. 2009).

Nuclear disks can develop a warped shape through several mechanisms. Very close to the center, the dragging of inertial frames by a rotating black hole (Lense & Thirring 1918) causes precession of a planar disk, if it is inclined to the plane perpendicular to the black hole's spin. Internal viscous torques try to align the disk angular momentum with the black hole angular momentum. Beyond a transition radius, the disk does not feel the effect of the black hole and remains at its initial inclination, while inside this radius the alignment proceeds. Hence the disk becomes warped [the Bardeen & Petterson (1975) effect]. Natarajan & Armitage (1999) showed that for black holes with masses of order 10^8 M$_\odot$ and accretion rates close to the Eddington limit the alignment time scale is short ($t \leqslant 10^6$yr). Application of this effect to the warped disks of NGC4258 and NGC1068 shows that the alignment radius lies well inside the observed positions of the maser spots, and models can be constructed that fit the observed warps rather well (Caproni et al. 2007; Martin 2008).

When a warped disk is exposed to radiation from a central source, or from its own inner portions, it is not illuminated isotropically. If it is also optically thick, the emission received at each position and re-radiated perpendicular to

---

* E-mail: siddiki@mpe.mpg.de, gerhard@mpe.mpg.de, marnabol @eso.org

the local disk plane induces a torque on the disk, and the warp is modified (Petterson 1977). Perturbations to planar disks can therefore cause radiation driven warping (Pringle 1996). Assuming a radiative efficiency $\epsilon \sim 10^{-2}$, and a black hole mass of 10^8 M$_\odot$, an initially flat disk is prone to warping beyond $r \geqslant 0.1$ pc, when the vertical and radial viscosity coefficients are comparable (Pringle 1997). Maloney et al. (1996) studied the stable and unstable modes of radiatively excited linear warps and found that the warp in NGC4258 may be explained by this mechanism only if the radiative efficieny is high.

Warps generated by gravitational interactions have been investigated mainly in the galactic context. Hunter & Toomre (1969) studied the linear bending waves of a self-gravitating, isolated, thin disk. They showed that such a disk permits long-lasting bending modes only when its surface density near the outer radius is truncated sufficiently fast, but not when realistic smooth edges are considered. This suggested interactions with nearby companion galaxies as a likely cause of warp excitation. Later, as the evidence for dark matter halos around galaxies became stronger, modelers developed scenarios in which the disk assumes the shape of a normal mode in the potential of a flattened dark halo (Sparke 1984; Kuijken 1991). However, subsequent work showed that these modes are damped quickly when the internal dynamical response of the halo is taken into account (Nelson & Tremaine 1995; Binney et al. 1998). Today, it seems most plausible that galactic warps result from interactions and from accretion of material with misaligned angular momentum (Jiang & Binney 1999).

On nuclear disk scales, Papaloizou et al. (1998) studied in linear theory the evolution of a thin self-gravitating viscous disk interacting with a massive object orbiting the central mass, with application to NGC4258. They concluded that the warp in the maser disk of NGC4258 might have been excited by a binary companion with a mass comparable to or higher than that of the maser disk. Their model also suggests a small twist (i.e. varying line-of-nodes) due to viscosity. Nayakshin (2005) considered the case of a non-self-gravitating disk perturbed by a massive ring. Employing the gravitational torques in the linear regime, he evaluated the precession induced by the ring on the disk elements. When the self-gravity of the disk is not taken into account, the rings precess differentially, which tends to destroy the disk structure.

Can models of warped nuclear disks be generalized to the fully non-linear regime? And assuming that the observed warps in galactic nuclei have been excited by one of the mechanisms discussed above, can the disk self-gravity maintain the warp even after the exciting torque has ceased to exist? As a first step towards answering these questions, the goal of the present paper is to investigate the possibility of steadily precessing, stable, non-linearly warped self-gravitating disks in the (Keplerian) gravitational potential of a massive black hole. In the following sections, we use a simple circular orbit ring model to find stable warped equilibria for systems with 2, 3, and many rings, assuming that the self-gravity of the rings provides the only acting torques.

2 STEADILY PRECESSING WARPED DISKS AND THEIR SCALING RELATION

2.1 Cold Disk Model and Equations of Motion

We consider a cold disk in which stars or gas are assumed to move on very nearly circular orbits. Following similar analysis of galactic warps (e.g., Toomre 1983, Sparke 1984, Kuijken 1991) we model such a disk as a collection of concentric circular rings. The orbital motion in the disk is maintained by the central black hole, and the self-gravity of the disk causes the rings to precess around the total angular momentum direction. Each ring may represent a set of stars or gas elements uniformly spread around their circular orbit. Moreover, when the precession frequency arising from the self-gravity of the disk is small compared to the orbital frequency of motion, the orbital parameters of single stars change only slowly and so one can average over the orbital motion. In this case, also the force exerted by a single star or mass element on the rest of the disk can be replaced by the force due to a ring of material spread over the orbit (Goldreich 1966).

Any of the rings is characterized by its mass m_i, radius r_i, inclination angle θ_i with respect to the reference plane, and azimuthal angle ϕ_i where the line-of-nodes cuts this plane. Later we will identify the reference plane as the plane perpendicular to the total angular momentum vector. The Lagrangian $\mathcal{L}_i$ of ring i is given by (Goldstein et al. 2002):

$$\begin{aligned}\mathcal{L}_i \;=\; & \frac{m_i r_i^2}{4}(\dot\theta_i^2 + \dot\phi_i^2 \sin^2\theta_i) + \frac{m_i r_i^2}{2}(\dot\psi + \dot\phi_i\cos\theta_i)^2 \\ & - V(r_i,\theta_i,\phi_i). \end{aligned} \tag{1}$$

The first two terms in equation (1) represent the kinetic energy of the motion T_i, $V(r_i,\theta_i,\phi_i)$ represents the gravitational potential energy, the Lagrangian is $\mathcal{L}_i = T_i - V_i$, and the energy of a ring is $E_i = T_i + V_i$. ψ is the position of a point on the ring, measured from the ascending node; (θ,ϕ,ψ) are Euler angles. The angular momentum of the motion along the ring

$$p_{\psi_i} = m_i r_i^2 \Omega(r_i) = m_i r_i^2(\dot\psi + \dot\phi_i\cos\theta_i) \tag{2}$$

is conserved since $\mathcal{L}_i$ does not depend on the coordinate ψ. The other momenta are the p_{ϕ_i}, the angular momentum around the $z-$direction, and p_{θ_i}, the angular momentum around the line of nodes. The equations of motion are:

$$p_{\theta_i} = \frac{m_i r_i^2}{2}\dot\theta_i, \tag{3}$$

$$p_{\phi_i} = \frac{m_i r_i^2}{2}\dot\phi_i \sin^2\theta_i + p_{\psi_i}\cos\theta_i \tag{4}$$

$$\dot p_{\theta_i} = \frac{m_i r_i^2}{2}\dot\phi_i{}^2 \sin\theta_i\cos\theta_i - \dot\phi_i p_{\psi_i}\sin\theta_i - \frac{\partial V(r_i,\theta_i,\phi_i)}{\partial\theta_i} \tag{5a}$$

$$= -\frac{\partial V(r_i,\theta_i,\phi_i)}{\partial\theta} - 2\,\frac{(p_{\phi_i} - p_{\psi_i}\cos\theta_i)(p_{\psi_i} - p_{\phi_i}\cos\theta_i)}{m_i r_i^2 \sin^3\theta_i} \tag{5b}$$

$$\dot p_{\phi_i} = -\frac{\partial V(r_i,\theta_i,\phi_i)}{\partial\phi_i} \tag{6}$$

and the Hamiltonian is:

$$\mathcal{H}_i = \frac{p_{\theta_i}^2}{m_i r_i^2} + \frac{1}{2}\frac{p_{\psi_i}^2}{m_i r_i^2} + \frac{(p_{\phi_i} - p_{\psi_i}\cos\theta_i)^2}{m_i r_i^2 \sin^2\theta_i} + V(r_i, \theta_i, \phi_i). \tag{7}$$

2.2 Components of $V(r, \theta, \phi)$, and Evaluation of the Torques

The gravitational potential energy, $V(r, \theta, \phi)$, has two components. One arises due to the central black hole, and is simply

$$V_{bh} = -\frac{G m_i M_{bh}}{r_i}. \tag{8}$$

at the position of the ring. The other component is the potential term V_m arising from the interaction of the ring under consideration with all other rings. We follow the description of Arnaboldi & Sparke (1994), using the derivation of Binney & Tremaine (1987) (Section 2.6.2), to evaluate the torque arising from the ring interactions.

The gravitational potential due to a circular ring of mass m_i and radius r_i in the $(\tilde{x}, \tilde{y})$ plane is

$$\Phi(\tilde{x}, \tilde{y}, \tilde{z}) = -\frac{2 G m_i}{\pi}\frac{K(k)\sqrt{(1 - k^2/2)}}{\sqrt{(r^2 + r_i^2)}}, \tag{9}$$

where

$$k^2 = \frac{4 R r_i}{(r^2 + r_i^2 + 2 R r_i)}. \tag{10}$$

Here $K(k)$ is the complete elliptic integral of the first kind, and R is the cylindrical radius $R^2 = \tilde{x}^2 + \tilde{y}^2$, so that $R^2 = r^2 - \tilde{z}^2$. A second ring of radius r_j at an angle α_{ij} to the first ring follows a curve $\tilde{z} = r_j \sin\alpha_{ij} \sin\psi$, where ψ runs between 0 and 2π. The mutual potential energy is

$$V_{ij}(\alpha_{ij}) = -\frac{G m_i m_j}{\pi^2 (r_i^2 + r_j^2)^{1/2}} \int_0^{2\pi} K(k)\sqrt{1 - k^2/2}\, d\psi \tag{11}$$

where m_j is the mass of the second ring, and k depends on r_i/r_j, $\sin\alpha_{ij}$ and ψ. The angle α_{ij} between the two rings is given by

$$\cos\alpha_{ij} = \cos\theta_i \cos\theta_j + \sin\theta_i \sin\theta_j \cos(\phi_i - \phi_j), \tag{12}$$

which reduces to $\cos\alpha_{ij} = \cos(\theta_i - \theta_j)$ when the line-of-nodes are aligned ($\phi_i = \phi_j$). The torque between the two rings (i, j) is

$$\frac{\partial V_{ij}}{\partial \alpha_{ij}} = \frac{G m_i m_j r_i r_j \sin 2\alpha_{ij}}{(r_i^2 + r_j^2)^{3/2}}\, I_{ij}(\alpha_{ij}, r_i/r_j), \tag{13a}$$

$$\begin{aligned} I_{ij} \quad \equiv \quad & \frac{4}{\pi^2}\int_0^{\pi/2}\left[\frac{E(k)(1 - k^2/2)}{(1 - k^2)} - K(k)\right] \\ & \times \frac{(1 - k^2/2)^{3/2}}{k^2}\frac{\sin^2\psi\, d\psi}{\sqrt{1 - \sin^2\alpha_{ij}\sin^2\psi}}. \end{aligned} \tag{13b}$$

We use the numerical program of Arnaboldi & Sparke (1994) for evaluating the integrals in this expression. The torques with respect to the angles (θ_i, ϕ_i) follow from multiplying equation (13a) by $\partial\alpha_{ij}/\partial\theta_i$ or $\partial\alpha_{ij}/\partial\phi_i$. In the following, we will write $V_{m,i} \equiv \sum_{j \neq i} V_{ij}$ for the potential energy of ring i due to the other rings, so that its *total* potential energy becomes $V(r_i, \theta_i, \phi_i) = V_{bh}(r_i) + V_{m,i}$. For further reference we also define $M_{ij} \equiv -\partial V_{ij}/\partial\theta_i$, and $M_{G,i} \equiv -\partial V_{m,i}/\partial\theta_i$ for the total gravitational torque on ring i around its line-of-nodes.

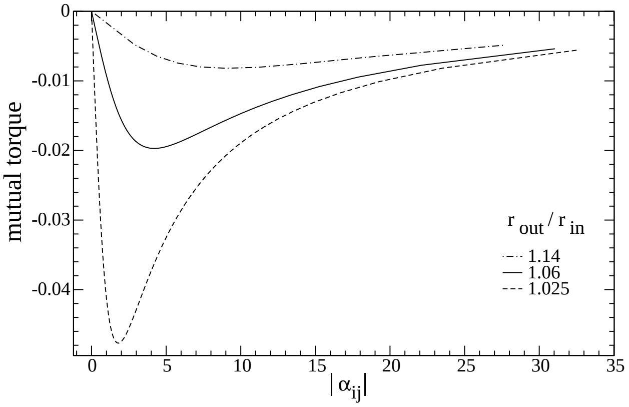

Figure 1. The mutual torque between two neighboring concentric rings, whose radii r_{out} and r_{in} are in the ratio ν as specified on the plot. The linear regime is limited to the left of the peak amplitude in these curves.

Figure 1 shows the torque between two rings with radii in the ratio $\nu \equiv r_{\text{out}}/r_{\text{in}}$ as a function of their mutual inclination α. The maximum of the torque occurs at very small angles, as noted previously by Kuijken (1991) who gives the approximation $\alpha_{\max} \simeq 1.2|\nu - 1|$. Only for $\alpha < \alpha_{\max}$ can the mutual torque be approximated as a linear function of α. Thus solutions $\theta(r)$ for the warp shape in linear theory can be scaled by a constant multiplicative factor only so long as the local gradient $d\theta/dr < 1.2/r$. Otherwise the local self-gravity torques of the disk are no longer able to maintain the linear theory warp shape, the non-linear equations must be used, and the shape of the warp must change.

2.3 Steadily Precessing Equilibria

A configuration of inclined rings precessing as a rigid body with constant $\dot{\phi}$ will in the following be denoted as a steadily precessing equilibrium, or equilibrium for short. In earlier works by Hunter & Toomre (1969); Sparke (1984), and Sparke & Casertano (1988) it was found that the eigenfrequencies of linear m=1 warp modes are purely real. Papaloizou et al. (1998) showed that this is a consequence of the self-adjointness of the operator in the tilt equation when there are no viscous or non-conservative forces. Then the eigenvectors are also real and thus the warp has a straight line-of-nodes and no spirality[1]. In the light of these linear theory results our effort will also be to find equilibria where all the rings have the same azimuth ϕ. The condition that all rings maintain constant inclination, $\dot{\theta} = 0$, implies also $\dot{p}_\theta = 0$, and for a given precession rate $\dot{\phi}$, the simultaneous solution of this equation for each of the rings determines the inclination angles, i.e. the equilibrium shape corresponding to this value of $\dot{\phi}$. We note that for $\dot{\phi} = 0$ equations (5a) admit a trivial tilt solution $\theta_i = \text{const.}$ but will assume $\dot{\phi} \neq 0$ in what follows.

---

[1] The line-of-nodes for a set of orbits is here defined as the union of points where all inclined orbits ($\theta_i \neq 0$) with respect to the reference plane intersect this plane.

From equations (5a) and (2) we can solve for the precession rate of ring i:

$$\dot{\phi}_i = \frac{\Omega_i}{\cos\theta_i} \pm \sqrt{\frac{\Omega_i^2}{\cos^2\theta_i} + \frac{2}{m_i r_i^2 \cos\theta_i \sin\theta_i} \sum_j \frac{\partial V_{ij}}{\partial \theta_i}} \tag{14}$$

when $\theta_i \neq 0$. Here $\Omega_i = \sqrt{GM_{bh}/r_i^3}$ is the angular velocity of particles on the ring around the black hole, and the term $\sum_j \partial V_{ij}/\partial\theta_i$ is the torque on ring i caused by all other rings j. The precession rate can therefore be fast or slow, corresponding to the plus and minus signs in this expression. When the interaction potential V_{ij} increases away from the plane $\theta = 0$, the second term in the square root is positive, so that the slow precession is retrograde ($\dot{\phi} < 0$). In the remainder of this paper we focus on such slow retrograde precession.

The components of angular momentum along the original (x, y, z) axes for a single ring read:

$$l_{x_i} = p_{\theta_i} \cos\phi_i + \frac{\sin\phi_i (p_{\psi_i} - p_{\phi_i}\cos\theta_i)}{\sin\theta_i}, \tag{15}$$

$$l_{y_i} = p_{\theta_i} \sin\phi_i - \frac{\cos\phi_i (p_{\psi_i} - p_{\phi_i}\cos\theta_i)}{\sin\theta_i}, \tag{16}$$

$$l_{z_i} = p_{\phi_i}. \tag{17}$$

Let us assume that we have found a precessing equilibrium from solving equations (3-6), with $p_{\theta_i} = 0$, $\dot{p}_{\theta_i} = 0$, and $p_{\phi_i} = \text{const.}$, $\dot{\phi} = \text{const.}$, $\phi_i = \phi$. Inserting equations (5a) and (4) into the expression for l_{x_i}, simplifying and summing over all rings gives the total angular momentum

$$l_x = \sum_i l_{x_i} = -\frac{\sin\phi}{\dot{\phi}} \sum_{i \neq j} \frac{\partial}{\partial\theta_i} V_{ij} = 0 \tag{18}$$

which sums to zero because for each pair of rings with interaction potential V_{ij} the torques are equal and opposite. Similarly, the total $l_y = 0$. Thus the total angular momentum of such a precessing equilibrium configuration is parallel to the z-axis. By construction, the angular momentum of the precession alone is also along the z-axis, i.e., the disk precesses around the total angular momentum vector axis.

For a uniformly precessing configuration, additional insight may be obtained by moving to a coordinate system which rotates around the angular momentum axis with the disk's precession frequency $\dot{\phi}$ (Kuijken 1991). In this reference frame the shape of the precessing disk is stationary, but the particles in the different rings still spin about their rings' symmetry axes. If the particles in ring i rotate with velocity $\Omega(r_i) r_i$ in the positive sense, they experience a Coriolis force in the rotating system which, integrated over the ring, results in a Coriolis torque on ring i along the p_θ-axis (line-of-nodes), given by

$$M_{C,i} = -m_i r_i^2 \Omega(r_i) \dot{\phi} \sin\theta_i. \tag{19}$$

For $0 < \theta < \pi/2$ and negative $\dot{\phi}$ this torque is along the positive p_θ-axis, i.e., is trying to retard the ring relative to the rotating frame. Because the retrograde precession speeds are small, we can neglect the centrifugal force terms. In this case, a stationary precessing configuration is obtained when the forward gravity torques and the retarding Coriolis torque balance in the rotating frame.

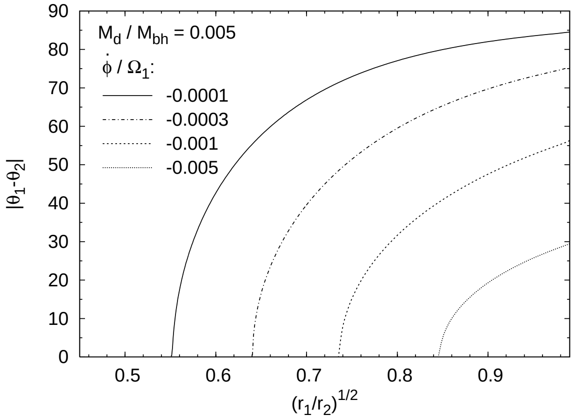

Figure 2. Relative inclination of two rings precessing together around a central mass M_{bh}, as a function of the square root of the ratio of their radii. The combined mass of the two rings is 0.5% of the central mass, approximately as in the Galactic center. The different curves are for various values of the precession frequency of the two-ring system, in units of the Keplerian frequency at r_1.

2.4 2-Ring and 3-Ring Cases

The argument just described suggests that there should exist steadily precessing 2-ring configurations in which one ring is tilted above the plane $\theta = 0$ and a second ring is tilted below this plane. Both rings are pulled towards $\theta = 0$ by the gravitational force from the other ring. The resulting gravity torques cause the angular momentum vectors of the two rings to precess in the same sense, and are balanced by the Coriolis torques in the precessing frame. To find such configurations we need to solve $\dot{p}_\theta = 0$ using eq. (5a) for both rings simultaneously. Assuming $\dot{\phi} \ll \Omega$, we can neglect terms of order $\dot{\phi}^2$; then using eq. (2) the equation for the inner ring at r_1 becomes

$$\sin\theta_1 \simeq -\frac{\partial V_{12}}{\partial\theta_1} / m_1 r_1^2 \Omega(r_1) \dot{\phi} \tag{20}$$

and the ratio of the two equations is

$$\sin\theta_1 / \sin\theta_2 \simeq -m_2 r_2^2 \Omega(r_2) / m_1 r_1^2 \Omega(r_1), \tag{21}$$

where m_1, m_2 are the two ring masses, r_1, r_2 their radii, θ_1, θ_2 their inclinations, and V_{12} the interaction potential. Given the ring masses and radii and θ_1, say, we can determine from these equations θ_2, the interaction potential, and thus finally the precession rate $\dot{\phi}$ required for steady precession.

Using the expression in (13a) for the torque between the rings, equation (20) can be cast into a more useful form:

$$\frac{\dot{\phi}}{\Omega_1} = -\frac{\sin 2\alpha \; I_{12}(\alpha, \nu)}{\sin\theta_1} \frac{\nu\mu}{(1+\nu^2)^{3/2}} \frac{m_1}{M_{bh}}, \tag{22}$$

where the angle $\alpha = \theta_1 - \theta_2$, $\nu \equiv r_2/r_1$, $\mu = m_2/m_1$, and I_{12} denotes the integral expression of equation (13b).

Figure 2 shows the difference $\theta_1 - \theta_2$ between the inclination angles of the two rings versus the square root of the

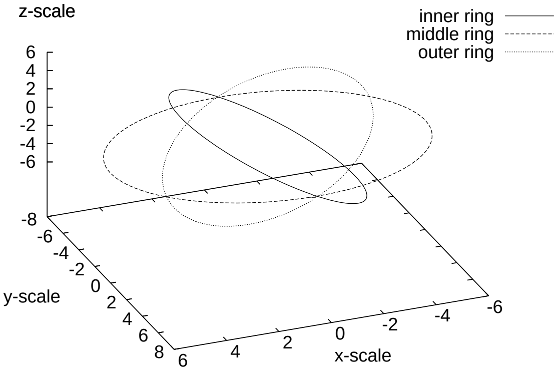

Figure 3. 3D view of a 3-ring system. The middle ring lies close to the equator, while the others are distributed almost symmetrically around it.

ratio of their radii, r_1/r_2, for different precession frequencies, expressed in units of the Keplerian frequency at r_1. The combined mass of the two rings is chosen to be 0.5% of the central mass, approximately as inferred for the system of two stellar rings in the Galactic center (Genzel et al. 2003). $\theta_1 - \theta_2$ increases with decreasing precession speed when the mass ratio is fixed. Eq. (22) shows that the same precessing equilibrium configuration can be obtained by changing $\dot{\phi} \propto M_d = m_1 + m_2$ and leaving all other parameters unchanged. More massive rings must precess faster for the same inclinations. Thus the sequence of curves in Fig. 2 can also be interpreted as a sequence of fixed precession frequency but with mass ratio M_d/M_{bh} increasing from bottom right to upper left.

Next consider three rings. In this case, each of the rings precesses in the potential of the other two rings, and the reference frame is defined by the common plane of precession perpendicular to the total angular momentum vector. Again $\dot{p}_\theta$ [eq. (5a)] should be zero at equilibrium for each of the rings. We can sum these three equations:

$$\sum_i^3 \dot{p}_{\theta_i} = \sum_{i=1}^3 \left(\frac{m_i r_i^2}{2} \dot{\phi}^2 \sin\theta_i \cos\theta_i - \dot{\phi} p_{\psi_i} \sin\theta_i \right) - \sum_{i=1}^3 \sum_{j \neq i} \frac{\partial V_{ij}}{\partial \theta_i} = 0. \quad (23)$$

The V_{ij} terms cancel since $\partial V_{ij}/\partial\theta_i = -\partial V_{ij}/\partial\theta_j$. The remaining terms can be rewritten as

$$\dot{\phi} \left(\sum_{i=1}^3 m_i r_i^2 \sin\theta_i \left[-\Omega(r_i) + \frac{1}{2}\dot{\phi}\cos\theta_i \right] \right) = 0, \quad (24)$$

making use of eq. (2). This shows that, apart from the no-precession solution, a steadily precessing equilibrium is possible only when at least one of the rings lies on the opposite side of the equator with respect to the others, i.e., has $\theta_i < 0$. Likewise the two rings of a precessing two-ring system must lie on opposite sides of the equator. Figure 3 shows as an example the 3D view of a 3-ring system with mass $M_d = 0.05 M_{bh}$ and $\dot{\phi} = -0.0021\Omega(r_2)$.

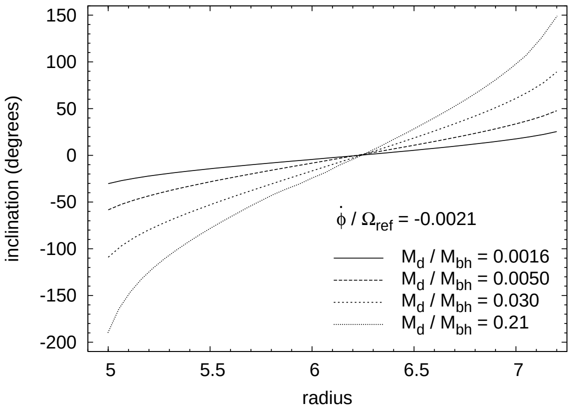

Figure 4. Inclination of a disk of constant surface density at different radii. The model consists of 35 rings precessing at a rate of $\dot{\phi} = -10^{-3}$ units, so that $\dot{\phi}/\Omega(r_{\rm ref}) = -0.0021$ on its middle (reference) ring. Each curve corresponds to a different M_d/M_{bh} mass fraction. The warp becomes more pronounced when the disk mass is increased. The smallest and highest masses correspond to the limits for stability (see Section 2.7).

2.5 Approximation of A Disk With n-Rings

We now consider a disk represented as a collection of n concentric rings. To find a precessing equilibrium, we solve $\dot{p}_\theta = 0$ (eqs. 5a) for all rings simultaneously, summing over the torques from all other rings (eqs. 13a). These are n equations for n+1 unknowns, the n inclinations θ_i and $\dot{\phi}$, which we solve keeping $\dot{\phi}$ fixed (Arnaboldi & Sparke 1994)[2]. Figure 4 shows a sequence of equilibria obtained for a constant surface density disk consisting of 35 rings. On each curve, the extent of the disk (*i.e.* $\Delta r = r_{\rm out} - r_{\rm in}$) is fixed at 2.2 units, and the precession rate is $\dot{\phi}/\Omega(r_{\rm ref}) = -0.0021$ where $\Omega(r_{\rm ref})$ is the circular frequency on the middle (reference) ring. The disk mass fraction M_d/M_{bh} varies from 0.16% to 21%. As the mass of the disk increases, the degree of warping increases dramatically so that the Coriolis torques can keep the balance of the gravity torques. The basic shape of the disk is similar to that of the system of three rings in Fig. 3. The middle rings lie closest to the equator, while the inner and outer rings are almost symmetrically distributed around it.

Obviously, the larger the number of rings the better the approximation to a continuous disk. Figure 5 shows the convergence of the total torques (upper panel), and of the inclination angles obtained in steadily precessing equilibrium (lower panel), for the innermost and outermost rings, when the number of rings to represent the disk is increased but the extent and the mass of the disk are kept fixed. One sees that quite a number of rings are needed before the torques converge. The inclination of the outer and inner rings have approximately converged when $n \gtrsim 30$.

---

[2] Note that this does not work in linear theory because the linear solution can be scaled arbitrarily, i.e., one of the θ_i can be eliminated.

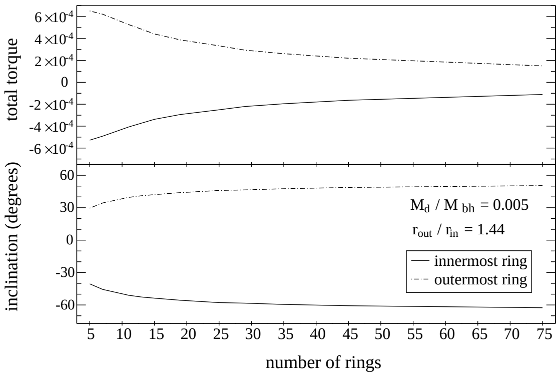

Figure 5. Convergence of the total torques (upper panel), and inclinations (lower panel), for the innermost (solid lines) and outermost rings (dot-dashed lines), when the number of rings to represent the disk is increased but the extent and the mass of the disk are kept fixed.

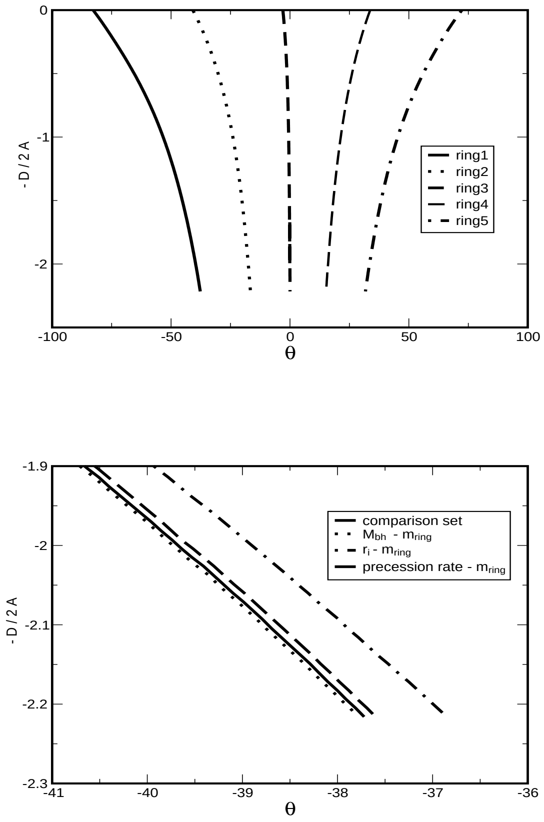

Figure 6. Top: Values $-D_i/2A_i$ (eq. 28) for a system of 5 rings with the parameters described in the text. The absolute value of the precession speed increases along the curves from top to bottom. Bottom: Parameter scaling of this system according to eq. (28). This figure shows a zoom into the region where the orientation of the 1^{st} ring predicted by the scaling deviates from the orientation in the original 5 ring model (shown as the solid line). Dots show when the black hole mass is increased by a factor of 4 and the ring mass is increased by a factor of 2, the dotted-dashed line shows when the radius is increased by a factor of 4 and ring mass by a factor of 8, and the long dashed line shows when the scaling is done by increasing the precession rate by a factor of 2 while increasing again the ring mass by a factor of 2.

2.6 Scaling the Solutions

Now we go back to the equilibria themselves, in particular to the question of their scaling properties. When the torque on ring i from all other rings is decomposed as

$$M_{G,i} = -\sum_j \frac{\partial V_{ij}}{\partial \theta_i} = -\sum_j \frac{\partial V_{ij}}{\partial \alpha_{ij}} \frac{\partial \alpha_{ij}}{\partial \theta_i}, \qquad (25)$$

the mass- and radius-dependent part is the first derivative on the r.h.s. The second factor in each term of this sum depends from equation (12) only on the two sets of angles θ_i, ϕ_i, θ_j, ϕ_j. For equilibria with a common precessing line-of-nodes, $\alpha_{ij} = (\theta_i - \theta_j)$, so the derivative is always unity. For the potential derivative terms, we use equation (13a) and express all ring masses and radii in terms of the mass and radius of a reference ring, i.e., we write $\mu_i \equiv m_i/m_{\rm ref}$, $\nu_i \equiv r_i/r_{\rm ref}$, and similar for j. Then (25) takes the form:

$$M_{G,i} = -\frac{G m_{\rm ref}^2}{r_{\rm ref}} \underbrace{\left[\sum_j \frac{\mu_i \mu_j \nu_i \nu_j \sin\alpha_{ij}}{(\nu_i^2 + \nu_j^2)^{3/2}} I_{ij}(\alpha_{ij}, \nu_i, \nu_j) \right]}_{} \qquad (26)$$

where we denote the expression over the brace as $D_i/2$. For each precessing equilibrium disk configuration as in Fig. 4 D_i is a constant, and the torques on all rings scale as $\propto m_{\rm ref}^2/r_{\rm ref}$. If we now go back to equation (14), insert equation (26), and normalize the precession rate with the circular frequency at the reference radius, $\Omega_{\rm ref} \equiv (GM_{bh}/r_{\rm ref}^3)^{1/2}$, we find

$$\frac{\dot{\phi}_i}{\Omega_{\rm ref}} = \frac{1}{\nu_i^{3/2} \cos\theta_i} \left(1 \pm \sqrt{1 + \frac{\nu_i \cos\theta_i}{\mu_i \sin\theta_i} D_i \frac{m_{\rm ref}}{M_{bh}}} \right). \qquad (27)$$

For negative $\dot{\phi}$ and after a Taylor expansion of the term in the square root, appropriate for slow retrograde precession, equation (27) becomes

$$\frac{\dot{\phi}_i}{\Omega_{\rm ref}} \simeq -\frac{D_i}{2\mu_i \nu_i^{1/2} \sin\theta_i} \frac{m_{\rm ref}}{M_{bh}} \equiv -\frac{D_i}{2A_i} \frac{m_{\rm ref}}{M_{bh}}. \qquad (28)$$

A precessing equilibrium is one for which all rings precess with the same common frequency, $\dot{\phi}_i = \dot{\phi}$. Equation (28) thus shows that for a fixed precessing disk mass configuration (i.e., fixed ring masses, radii, and inclinations, hence fixed $D_i/2A_i$), the precession rate $\dot{\phi}$ scales proportional to the Keplerian frequency at some reference radius in the disk and proportional to the disk-to-black hole mass ratio. Vice versa, equation (28) can be interpreted as a scaling relation which says that a precessing equilibrium solution remains unchanged in shape (θ_i) under changes of the disk mass, disk radius, black hole mass, and precession rate, provided the ratio $(\dot{\phi}/\Omega_{\rm ref})/(M_d/M_{bh})$ is held constant.

Figure 6 depicts the values of $-D_i/2A_i$ for a system of 5 rings. The radii of the rings are calculated such that $r_i = \kappa^{i-1} \times r_1$, with $i = 1, 2, ..n$, $\kappa = 1.07$, $r_1 = 5.75$, and $n = 5$, so if the third ring is the reference ring, $\nu_i = \kappa^{i-3}$. The ring masses are assumed to all have the same value, 0.5516, so $\mu_i = 1$, the black hole has a mass of 51.16, and $M_d/M_{bh} = 0.054$. On each curve in Fig. 6, the precession rate $\dot{\phi}$ increases with steps of -5×10^{-5} ($\Delta\dot{\phi}/\Omega(r_3) = -1.18\times10^{-4}$) starting from a value of -1×10^{-4} (i.e., $\dot{\phi}/\Omega(r_3) = -2.4\times10^{-4}$) at the top. We checked the accuracy of the scaling and of our calculations by computing $-D_i/2A_i$ values for different parameter pairs of the system that should give the same $-D_i/2A_i$ according to equation (28). We overlay the results for the first ring and precession speed $\dot{\phi}/\Omega(r_3) = -0.0021$, in the lower panel of Fig. 6, zooming into the parameter region $-2.3 < D_1/2A_1 < -1.9$ where the different curves deviate from each other the most. In the worst case, due to the scaling of the ring radii, the deviations of the θ_i's from their values for the original 5 ring system are still less than 1°. Changes in radii cause the largest deviations from the scaling relation because of the way in which they enter in the quantity D_i (equation 27). The scaling results for the other rings are similar.

2.7 Stability

In this section we investigate the stability of the precessing equilibrium solutions found above. Hunter & Toomre (1969) proved that isolated thin self-gravitating disks are stable to all $m = 1$ warp perturbations and this carries over to disks embedded in spherical or oblate potentials (e.g. Sparke & Casertano 1988). We show here that the nonlinearly warped precessing disks can be both stable and unstable to general ring-like perturbations. We describe small perturbations of the precessing disk solutions by the linearized equations of motion around equilibrium:

$$\begin{aligned}
\Delta\dot{\theta}_i &= \frac{\partial^2 T_i}{\partial p_{\theta_i}^2}\Delta p_{\theta_i}, \\
\Delta\dot{\phi}_i &= \frac{\partial^2 T_i}{\partial p_{\phi_i}\partial\theta_i}\Delta\theta_i + \frac{\partial^2 T_i}{\partial p_{\phi_i}^2}\Delta p_{\phi_i}, \\
\Delta\dot{p}_{\theta_i} &= -\frac{\partial^2 T_i}{\partial\theta_i\partial p_{\phi_i}}\Delta p_{\phi_i} - \frac{\partial^2 T_i}{\partial\theta_i^2}\Delta\theta_i - \frac{\partial^2 V_{m,i}}{\partial\theta_i^2}\Delta\theta_i \\
&\quad -\frac{\partial^2 V_{m,i}}{\partial\theta_i\partial\phi_i}\Delta\phi_i - \sum_j \frac{\partial^2 V_{m,i}}{\partial\theta_i\partial\phi_j}\Delta\phi_j - \sum_j \frac{\partial^2 V_{m,i}}{\partial\theta_i\partial\theta_j}\Delta\theta_j, \\
\Delta\dot{p}_{\phi_i} &= -\frac{\partial^2 V_{m,i}}{\partial\phi_i\partial\theta_i}\Delta\theta_i - \frac{\partial^2 V_{m,i}}{\partial\phi_i^2}\Delta\phi_i \\
&\quad -\sum_j \frac{\partial^2 V_{m,i}}{\partial\phi_i\partial\theta_j}\Delta\theta_j - \sum_j \frac{\partial^2 V_{m,i}}{\partial\phi_i\partial\phi_j}\Delta\phi_j. \qquad (29)
\end{aligned}$$

Here T_i and $V_{m,i}$ are the kinetic and potential energy terms in the Hamiltonian (7) for ring i, respectively, and the partial derivatives are evaluated at the equilibrium solution ($\theta_i, \phi_i = \text{const.}, \dot{p}_{\theta_i} = 0, \dot{p}_{\phi_i} = 0$). These linear equations have solutions of the form $\mathrm{e}^{\lambda t}\Delta\theta_0, \ldots$ etc., where $\lambda = \lambda_{\mathcal{R}} \pm \mathrm{i}\lambda_{\mathcal{I}\mathrm{m}}$ with its real and imaginary parts. The (constant) coefficients of the Δ terms in equation (29) form a matrix H which carries the information on stability. When the real parts of the eigenvalues of the matrix H, $\lambda_{\mathcal{R}} = 0$, the imaginary parts of the eigenvalues, $\lambda_{\mathcal{I}m}$, constitute a rotation matrix through which the solutions oscillate around the precessing equilibrium with frequencies $\lambda_{\mathcal{I}m}$, and the equilibrium is said to be stable. When $\lambda_{\mathcal{R}} < 0$, the solutions spiral towards the unperturbed equilibrium positions, leading to asymptotic stability of the equilibrium. If, however, any of the eigenvalues have a nonzero real part, $\lambda_{\mathcal{R}} > 0$, the system moves away from equilibrium exponentially, and is unstable.

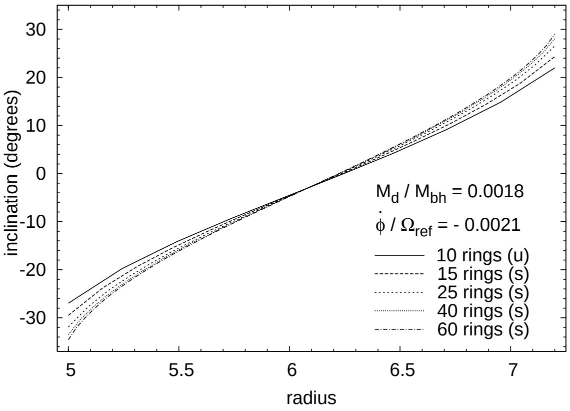

Figure 7. Change of the shape of a solution near the lower stable boundary of Fig. 4 with the number of rings used to represent the disk. The disk-to-black hole mass ratio, precession speed, and number of rings are given on the plot. The letters "u" and "s" in parentheses following the number of rings stand for unstable and stable solutions respectively.

For determining the stability of any of our precessing n-ring solutions, we compute the $4n \times 4n$ stability matrix H, using the equilibrium ($\theta_i, \phi_i = \text{const.}, \dot{p}_{\theta_i} = 0, \dot{p}_{\phi_i} = 0$). We then evaluate the eigenvalues of the matrix H, using routine F02EBF of the Numerical Algorithms Group (NAG). This routine is suitable for computing eigenvalues and optionally eigenvectors of real matrices.

First, we briefly discuss one example for the convergence of the linear stability results. In Section 2.5 we had already discussed the convergence of the gravitational torques, and of the inclination angles obtained for the precessing equilibrium solutions, as a function of the number of rings used to represent the disk (see Fig. 5). Figure 7 shows how the shape of a solution near the lower stable boundary of Fig. 4 and its stability changes with the number of rings used to represent the disk. The transition from unstable to stable occurs at a disk mass fraction of $M_d/M_{bh} = 0.0018, 0.0013, 0.0011, 0.0011$ for $n = 15, 25, 45, 75$ rings. This shows that the transition has approximately converged when $n \simeq 45$.

Next, we consider the issue of scaling. We have already seen that the equilibrium solutions can be scaled in radius, mass, and precession speed according to the approximate (but accurate) scaling relation (28): the angles θ_i for all rings in the disk remain unchanged if the precession speed expressed in units of the angular frequency scales linearly with the disk-to-black hole mass fraction. Figure 8 shows disks with $M_d/M_{bh} = 0.05$ consisting of equal mass rings with constant ratios of all ring radii relative to each other. Keeping the ratio $\dot{\phi}\sqrt{r_{\mathrm{ref}}^3}$ constant, we have moved the midpoints of these disks to various radii. All these configurations are stable, and actually represent a similar warped disk (i.e. innermost and outermost inclinations being the same) at different distances from the black hole.

Figure 9 illustrates the stability properties for these disks when the disk mass and precession speed are changed simultaneously. The boundaries of the stable solutions obtained for a fixed disk mass configuration, i.e., a configuration with constant ratios of all ring masses and radii relative to each other, are shown by the two dashed lines in

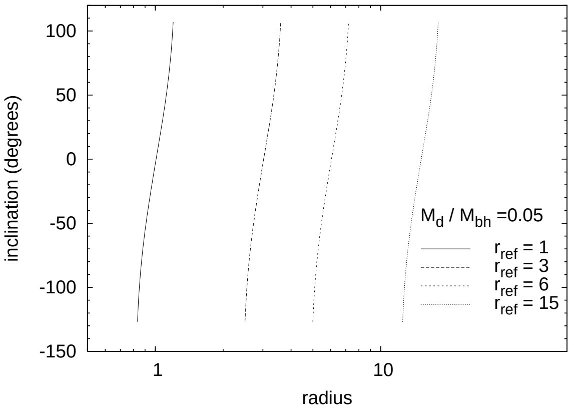

Figure 8. 35-ring-disks with constant $M_d/M_{bh} = 0.05$ but different sizes. The curves from left to right show warped disk solutions for which the scale radius $r_{\rm ref}$ is shifted to ever higher values while correspondingly $\dot\phi$ is decreased to keep $\dot\phi\sqrt{r^3_{\rm ref}}$ fixed. The innermost and outermost ring inclinations are identical for all disks, as expected from the scaling relation, and all rescaled disks are found to be stable.

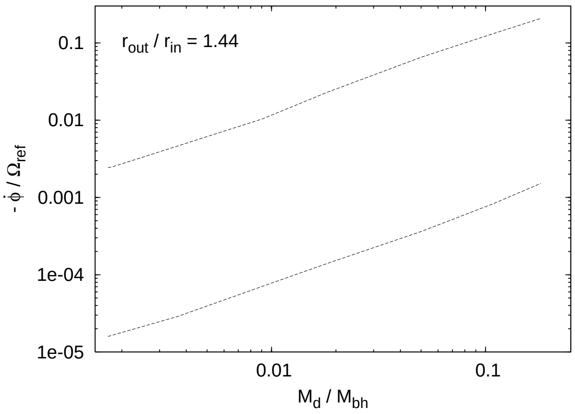

Figure 9. Schematic representation of stable warped disk solutions in the M_d/M_{bh} versus $\dot\phi/\Omega$ plane. The two inclined dashed lines enclose the stable region: the upper (lower) dashed line corresponds to the maximum (minimum) stable precession frequency at fixed disk-to-black hole mass ratio. This diagram is for disks with the same surface density profile and inner and outer boundaries $r_{\rm in}$, $r_{\rm out}$.

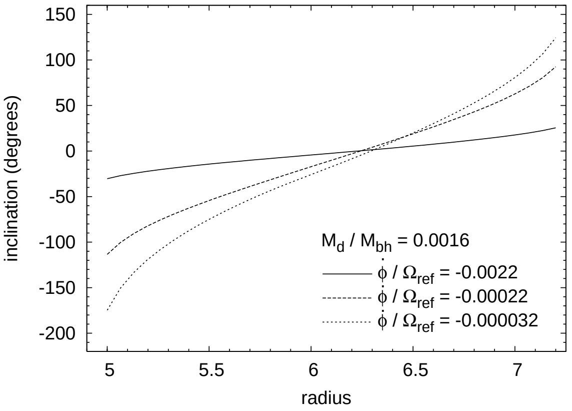

Figure 10. Inclination of a disk of 35 rings at different radii for $M_d/M_{bh} = 0.0016$. On each curve the precession frequency $\dot\phi$ has a different value, given on the figure in terms of the orbital frequency at the position of the middle ring. The upper and lower curves show the boundaries of stable solutions. See Section 2.7 and Fig. 9.

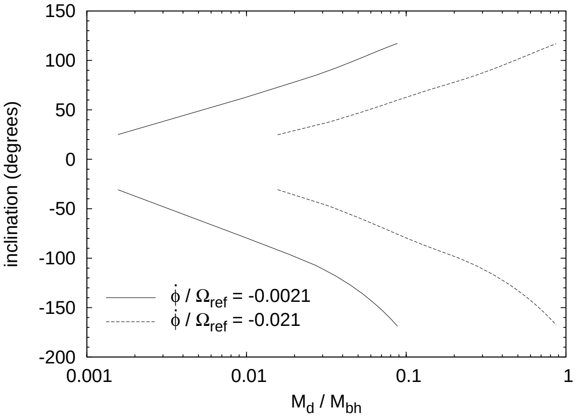

Figure 11. Variation with disk-to-black hole mass ratio of the inclinations of the outermost ($\theta > 0$) and innermost ($\theta < 0$) rings of a 35-ring warped disk with $r_{\rm out}/r_{\rm in} = 1.44$, for two different values of the precession frequency. The figure shows how the warping increases with increasing disk mass fraction and with decreasing precession speed, and also illustrates the scaling relation of equation (28). Up to numerical errors, the minimum and maximum values of θ are the same on all two curves.

the figure. All stable solutions lie between the two lines. These dashed lines are nearly straight, indicating that the minimum and maximum $\dot\phi/\Omega_{\rm ref}$ solutions at different mass fractions can be essentially scaled to eachother - if the same (scaled) equilibrium solution was the stability boundary for all mass ratios, the lines would reflect the scaling relation of eq. (27) respectively eq. (28) precisely.

Figure 9 shows that for each ratio of disk mass to black hole mass, there is a minimum and maximum stable precession speed $\dot\phi/\Omega$, and vice-versa. (see Fig. 4 and Section 3.1 below). The minimum (maximum) stable mass for given $\dot\phi/\Omega$ is stable for all precession speeds lower (higher) than the original $\dot\phi/\Omega$, until the other boundary curve is reached. For other disk mass configurations, the range of stable mass ratios and the corresponding boundary lines change, but the qualitative behaviour remains the same.

3 STEADILY PRECESSING, NON-LINEARLY WARPED KEPLERIAN DISKS: RESULTS

3.1 Warp Shapes and Warp Angles of Stable Precessing Disks

We have already seen in the discussion of three-ring and n-ring systems in Section 2 that self-gravitating precessing disks in a Keplerian potential can be strongly warped. In fact, some of the disks shown in Fig. 4 are so strongly warped that they would obscure the central black hole from most lines-of-sight.

In this section we discuss these results in more detail.

Figure 10 shows the warped stable equilibrium solutions obtained for a sequence of disks with varying precession frequency. These disks have constant surface density between fixed inner and outer radii, and a total disk-to-black hole mass ratio of $M_d = 0.0016 M_{bh}$. The solutions shown in Fig. 10 are all linearly stable, according to the analysis described in Section 2.7. Outside the range of models bounded by the upper and lower curves one can find further equilibria, but these are unstable.

By construction, these disks have a fixed line-of-nodes at all radii, and their shapes are given in terms of the inclination angle θ relative to the plane defined by the total angular momentum vector. In all cases there is a middle section of the disk which lies approximately in this plane, whereas the inner and outer parts warp away from this plane in opposite directions. For the most strongly warped stable solution in Fig. 10 the inner warp is by ~ 180 deg and the outer warp by ~ 120 deg. This is obtained for the lowest stable pattern speed, in accordance with the balance between gravitational and Coriolis torques [see Fig. 1 and equation (19)]: the torques are weakest for the large inclinations. This can be seen already in the two-ring problem [see equations (20) and (22)]. The least strongly warped disk solution in this example has inner and outer warps ∼25-30deg.

The variation of the maximum inner and outer warp angles with disk mass fraction is shown in Figure 11 for fixed precession frequency and radial extent of the disk. The curves with $\theta > 0$ represent the outermost ring inclinations, and those with $\theta < 0$ show the innermost ring inclinations for different precession speeds. As we have already seen in Figs. 4, 10, these inclinations increase with increasing disk mass fraction and with decreasing precession speed. Fig. 11 also illustrates the scaling relation of equation (28). Up to numerical errors, the different curves can be scaled on top of each other.

Some three-dimensional illustrations of warped disks from this family are shown in Figure 12. From top to bottom, these plots shows warped disks with increasing amplitude of the warp, such that the disk in the bottom panel of Fig. 12 completely encloses the central black hole.

3.2 Comparison with Linear Theory Solutions

Previous work on warped and twisted disks around black holes has often made use of the linear approximation, in which the inclination angles of all parts of the warped disk are assumed to be small. It is therefore interesting to briefly consider the linear limit of our analysis above.

For small warping angles α_{ij}, the self-gravity torques simplify considerably. Because the leading term in equation (13a) is already $O(\alpha_{ij})$, only the $O(1)$ part of the I_{ij} terms in this equation need to be included, while the next order, $O(\alpha_{ij}^2)$, can be neglected. Thus in computing I_{ij} the k^2 term for ring j in equation (10) can be approximated as:

$$k_{ij}^2 \approx \frac{4 r_i r_j}{(r_i + r_j)^2} \tag{30}$$

and the I_{ij} term can be integrated to give

$$I_{ij} \approx \frac{1}{\pi}\left[\frac{E(k_{ij})(1-k_{ij}^2/2)}{1-k_{ij}^2} - K(k_{ij})\right]\frac{(1-k_{ij}^2/2)^{3/2}}{k_{ij}^2}. \tag{31}$$

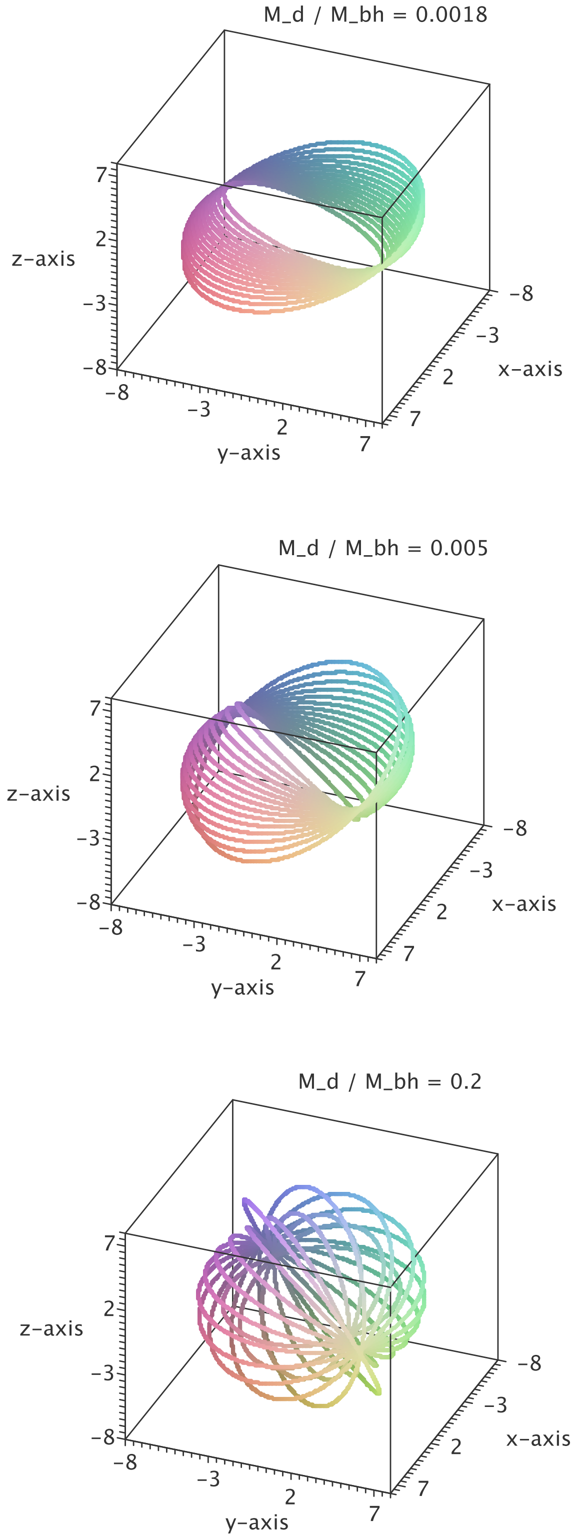

Figure 12. Three-dimensional views of several 15-ring disks similar to those shown in Fig. 4, with mass ratios given on the plots. The degree of warping increases with the disk mass fraction until (for disk mass fraction greater than 2 percent) the central black hole is completely hidden behind the warped disk.

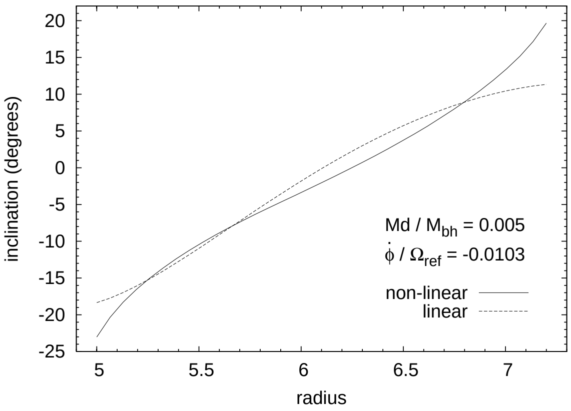

Figure 13. Warp shapes for a disk with $M_d/M_{bh} = 0.005$ as obtained in the linear (dashed line), and nonlinear (solid line) torques regimes, for the same precession speed. The linear mode is scaled to the maximal amplitude for which the linear approximation to the gravitational torques can be used. The non-linear disk shape is determined for the precession frequency given by the eigenvalue of the linear mode; it is unstable. Stable non-linear warps for this mass configuration have lower precession speeds and are more strongly warped than the solution shown.

The mutual torque on ring i from ring j becomes, to first order in α_{ij},

$$\frac{\partial V_{ij}}{\partial \theta_i} = \frac{\partial V_{ij}}{\partial \alpha_{ij}} \frac{\partial \alpha_{ij}}{\partial \theta_i} \approx \frac{2Gm_i m_j r_i r_j I_{ij} \alpha_{ij}}{(r_i + r_j)^{3/2}} \frac{\partial \alpha_{ij}}{\partial \theta_i}. \tag{32}$$

For a precessing equilibrium when $\phi_i = \phi_j$, $\alpha_{ij} = \theta_i - \theta_j$, the equation $\dot{p}_{\theta_i} = 0$ becomes to $O(\theta)$:

$$\dot{p}_{\theta_i} = \dot{\phi}^2 \frac{m_i r_i^2}{2} \theta_i - \dot{\phi} p_{\psi_i} \theta_i - \sum_{j=1}^{n} \frac{2Gm_i m_j r_i r_j I_{ij} (\theta_i - \theta_j)}{(r_i^2 + r_j^2)^{3/2}} = 0. \tag{33}$$

Equation (33) is a quadratic eigenvalue problem for the precession frequencies. When linearized, it transforms into a generalized eigenvalue problem of dimensions $2n \times 2n$. We use the NAG routine F02BJF to find the eigenvalues and eigenvectors of equation (33).

The $2n$ eigenvalues constitute two distinct families in the frequency spectrum of the disk; the fast prograde, and the slow retrograde frequencies. When sorted in decreasing order, the first retrograde frequency has a value of zero, and the associated eigenvector represents a tilt of the whole disk by the same angle, i.e. $\theta_i =$ constant. The next eigenvalue corresponds to the warps we have discussed so far where the disk has one radial node (modified tilt mode, Hunter & Toomre 1969; Sparke 1984; Sparke & Casertano 1988). In the following, we restrict our discussion to linear warp shapes of this kind.

In Figure 13 we show the modified tilt mode in linear theory of a disk with $M_d/M_{bh} = 0.005$, $r_{\rm in} = 5$ and $r_{\rm out} = 7.2$ for 40 rings. This is obtained by solving equation (33) and is shown with the dashed line. We note that in linear theory the warp shape can be arbitrarily scaled as long as the local gradient of the tilt satisfies $d\theta/dr < 1.2/r$ (see Section (2.2); if this condition is violated, the linear approximation to the self-gravity torques breaks down. Therefore in Fig. 13 the linear mode is scaled to its maximum possible amplitude such that the condition is everywhere satisfied.

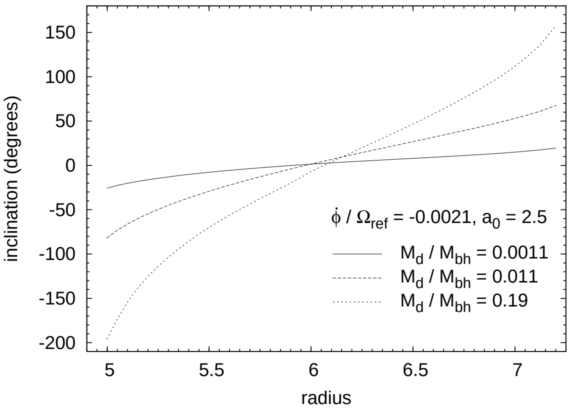

Figure 14. Inclination of a 35-ring-disk at different radii as in Figure 4, but for an exponential surface density profile with scale length $r_d = 2.5$. The precession speed is identical to that in Fig. 4. The upper and lower curves correspond to the limiting mass ratios for disk stability; see Section 2.7.

As mentioned above, the precession frequency of this mode is the first nontrivial eigenvalue in the retrograde family, and here it has a value of $\dot{\phi}/\Omega_{\rm ref} = -0.0103$ when normalized to the rotation frequency of the reference ring. For this frequency, we then solve equation (5a) to obtain the nonlinear warp shape shown by the solid line in Figure 13. The larger curvature of the non-linear warp near the inner and outer boundaries of the disk, with respect to the scaled linear mode, shows that the linear approximation overestimates the torques in these parts of the disk.

However, the main difference between linear modes and non-linear warps is that, for a given mass distribution of the disk (surface density profile, inner and outer boundaries), the precession frequency and shape of the modified tilt mode in linear theory is uniquely determined, whereas non-linear equilibrium warp solutions may exist for a range of precession frequencies and warp shapes or, e.g., for extended disks, may not exist at all. For the case shown in Fig. 13, non-linear warped equilibria are found for precession frequencies in the range $\dot{\phi}/\Omega_{\rm ref} = -8.87 \times 10^{-5} \rightarrow -1.16 \times 10^{-2}$ and are stable in the range $\dot{\phi}/\Omega_{\rm ref} = -9.24 \times 10^{-5} \rightarrow -9.63 \times 10^{-3}$. The particular non-linear warp shape obtained for the frequency of the linear mode and shown in Fig. 13 is unstable.

Alternatively, the warp shape may be parametrized by the inclination of the outermost ring, say, θ_n. Linear theory warps can in the previous example be considered valid up to $\theta_n \simeq 10^\circ$, and have all the same precession frequency. Non-linear warp modes are found in the range $\theta_n = 19.1^\circ \rightarrow 130^\circ$, and are stable in the range $\theta_n = 20.9^\circ \rightarrow 129^\circ$. They are disjunct in θ_n from the linear modes, and their precession speed decreases with θ_n according to the balance of gravitational and Coriolis torques.

3.3 Dependence on Surface Density Profile and Radial Extent

The warped disks presented in Figs. 4, 11 have constant surface density. For comparison, Figure 14 shows the warping of an exponential disk, with surface density $\Sigma(r) = \Sigma_0 \exp(-r/r_d)$ where Σ_0 denotes the central density and r_d

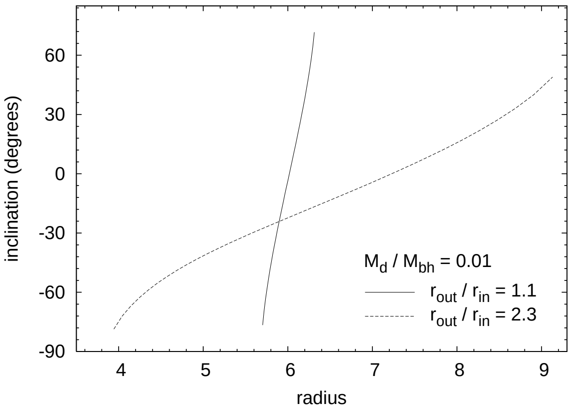

Figure 15. Stable warped equilibria for 35-ring-disks with constant surface density but varying radial extent, and with $M_d = 0.01M_{bh}$. The solid and dashed lines demarcate the boundaries of the region of stable solutions.

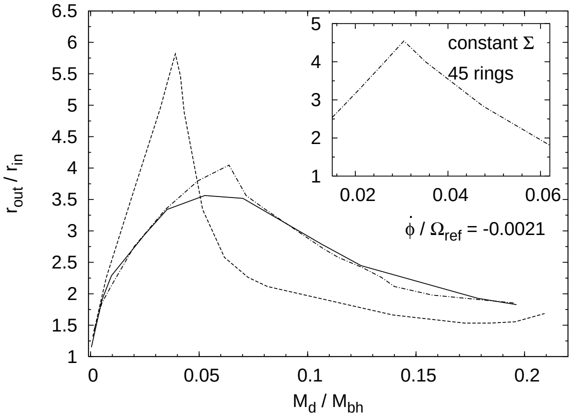

Figure 16. Maximum radial extent of stable warped disk equilibria $r_{\rm out}/r_{\rm in}$, as a function of disk-to-black hole mass ratio. The dashed line represents the result for a disk of 15 rings with constant surface density, the solid line is for an exponential disk with scale-length $r_d = 5.2$, and the dot-dashed line is for an exponential disk with scale-length $r_d = 2.5$. The inset shows results obtained for the constant surface density disks when instead approximated by 45 rings, near the mass ratio with maximum $r_{\rm out}/r_{\rm in}$. Typical ratios are $r_{\rm out}/r_{\rm in}$ =2-4.

is the scale length, chosen to be 2.5 units in this example. The other parameters (relative ring radii, precession speed) are identical to those used in Fig. 4. The basic warp shapes are similar as for constant surface density, but the maximum outer warp angles are slightly larger. The range of stable disk masses is also comparable to that for the constant surface density disk (for the same precession speed); see the curves showing the boundaries of stability in Figs. 4, 14.

Because the condition for a warped equilibrium is that the Coriolis and gravitational torques balance, clearly not only the mass fraction and mass distribution, but also the radial extent of the disk must be important for determining the warp shape and its stability. To investigate this we compiled a set of precessing equilibria with varying radius scaling factor κ, as follows (see also Section 2.5). After fixing the radius of the middle ring of the disk, $r_{\rm mid}$, we determine the remaining ring radii such that

$$r_i = r_{\rm mid}\kappa^j \begin{cases} j = i - \frac{n+1}{2} & n \text{ odd} \\ j = i - \frac{n}{2} & n \text{ even} \end{cases} \qquad i = 1, 2, \ldots, n \quad (34)$$

where n is the number of rings. For illustration, we consider a family of disk models with the same disk-to-black hole mass fraction $M_d = 0.01M_{bh}$, each with its own constant surface density given by M_d and κ. All disks are made of $n = 35$ rings, and the middle ring radius is set to $r_{\rm mid} = 6$ units.

Figure 15 shows precessing equilibria for such disks for different κ. The upper and lower curves show the two disk shapes that bound the stable range of solutions in terms of the κ-factor. In the case where the rings have minimum possible separation from each other, the inner ring has a radius of $r_1 = 5.7$ units, and the outer ring has $r_n = 6.3$ units. On the other hand, for the most extended stable disk in this family, $r_1 = 3.9$, and $r_n = 9.1$. When the extent of the disk is increased, a slight decrease in the warping is observed in Fig. 15. This is due to the fact that the torque from a ring of constant mass decreases with distance to the ring, cf. equation (13a).

Figure 16 shows the radial extent of the disk $r_{\rm out}/r_{\rm in}$ for which stable warped equilibria can be found, for different surface density profiles and as a function of disk-to-black hole mass ratio. The most important result of these calculations is that stable non-linear warps can be maintained only for disks with inner and outer boundaries, for which $r_{\rm out}/r_{\rm in} \simeq$ 2-4. This is reminiscent of the result of Hunter & Toomre (1969) that in linear theory only truncated disks permit long-lasting bending modes.

3.4 Time-Evolution of Ring Systems

In this section we consider the explicit time-evolution of a precessing system of self-gravitating rings in a massive black hole potential. By integrating the equations of motion, equations (3)-(6), starting from initial conditions corresponding to one of the precessing disk solutions found earlier, we can check the stability of this solution directly and compare with the linear stability analysis.

In these integrations, we use disks of 20 equal mass rings, equally spaced in radius. The ratio of the outermost ring radius to that of the innermost ring is 1.44. The initial θ_i are obtained from precessing equilibrium solutions; all rings have the same line-of-nodes, i.e., the same initial ϕ_i. The equilibrium precession speed is given by $\dot{\phi}/\Omega_{\rm ref} = -0.0021$.

In the following figures, symbols starting from the outer circle show the variation of inclination θ with ring radius, where the ring radii are shown as distances from the center of the plot, with scale shown on the lower right. The symbols starting from the inner circle show how the azimuthal angle ϕ changes with the ring radius; for this part of the plot, the ring radii are scaled down to the half of their values to make the figure more easily readable. The elapsed time of the integration is shown on top of the figures, in terms of the number of orbital periods at the position of the outermost ring n where $\dot{\phi}/\Omega_n = -0.0027$.

Figure 17 shows the time evolution of a disk of 20 rings with $M_d = 0.05M_{bh}$. The disk stays in equilibrium for 12 orbital periods, consistent with its linear stability. Figure 18

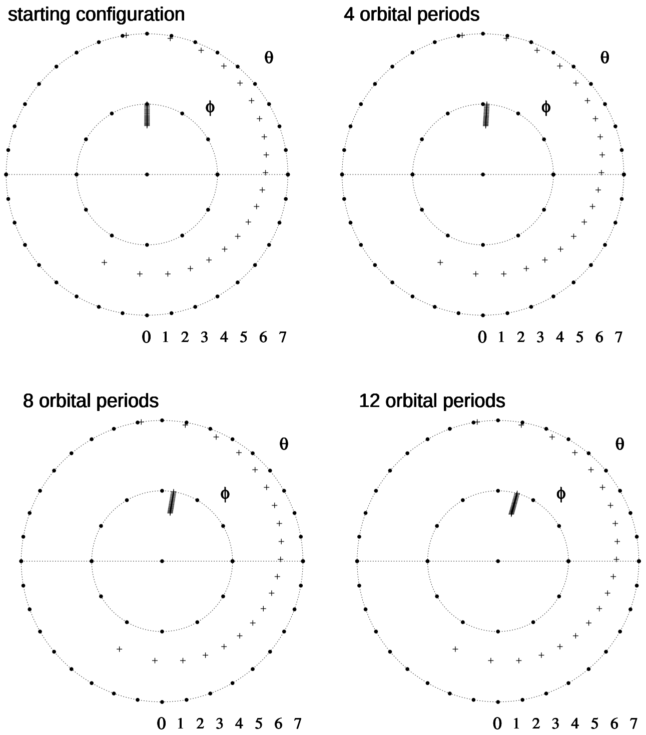

Figure 17. Time-evolution of a disk of 20 rings with total mass $M_d = 0.05 M_{bh}$. The disk is stable.

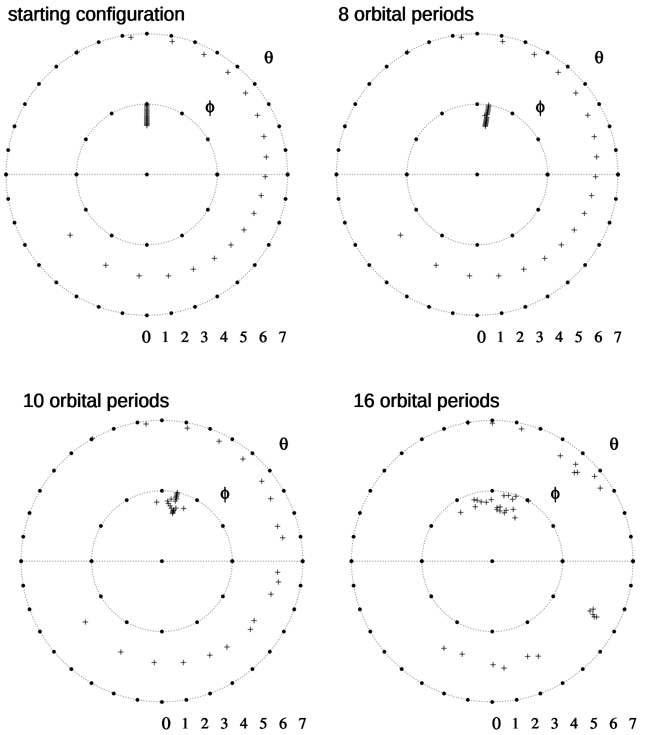

Figure 18. Time evolution of a disk of 20 rings with total mass $M_d = 0.1 M_{bh}$. The disk precesses as a unit for nearly 8 orbital periods, but then it starts to break up, so is unstable.

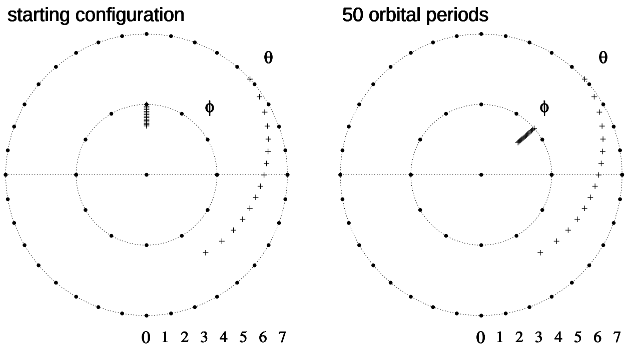

Figure 19. Time-evolution of a disk of 15 rings with mass fraction $M_d/M_{bh} = 0.005$. The disk is followed for 50 orbital periods and is stable.

shows the evolution of disk of 20 rings with $M_d = 0.1 M_{bh}$. This disk precesses as a unit for 8 orbital periods, but then it starts to break into parts, hence the disk is unstable, as also predicted by linear stability analysis.

To strengthen the agreement between linear stability and time evolution results, we integrate two of these ring systems for longer. Figures 19 and 20 show the time evolution of two disks with masses $M_d = 0.005 M_{bh}$ and $M_d = 0.02 M_{bh}$, with 15 logarithmically spaced rings according to equation (34), over 50 orbital periods. In both cases the disks are stable, as expected from the linear stability analysis.

4 DISCUSSION

4.1 Theoretical Issues

In this work we have considered warped disks around black holes for which the only acting force is gravity and the disk is approximated as a nested sequence of circular rings. We have focussed on non-linearly warped, steadily precessing disk configurations, contrary to most previous work in which small amplitude warps were considered, often of a transient nature. We have found that stable, steadily precessing, highly warped disks can be constructed, albeit only over a limited radial range, such that the typical ratio of the outer to the inner boundary radius is ∼ 2-4.

In one illustrative case, we have compared with a linear theory warped disk. For a given disk mass configuration, the precession frequency of the linear, modified tilt mode is given as an eigenvalue, and the shape can be scaled up to the amplitude where the validity of the linear approximation to the gravitational torques breaks down. The corresponding non-linear warp with the same precession frequency is unstable. Stable non-linear warps for the same mass configuration exist for a disjunct range of precession speeds which are all slower than that of the linear mode. Their warp angles increase with decreasing precession speed, and the non-linear solutions are more strongly warped than the linear mode at the maximum scaling.

These warped disks obey a scaling relation in the sense that (i) they can be scaled to an arbitrary radius r, provided the precession speed is scaled to the circular frequency $\Omega(r)$, and (ii) they can be scaled in mass, provided the ratio of precession frequency to $\Omega(r)$ keeps in line with the ratio of disk mass to black hole mass.

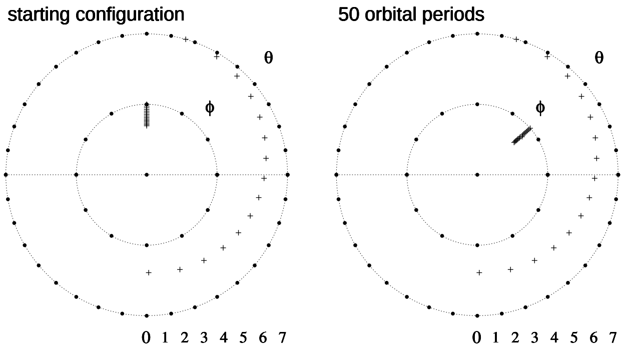

Figure 20. Time-evolution of a disk of 15 rings with mass fraction of $M_d/M_{bh} = 0.02$. The evolution is followed for 50 orbital periods and the disk is stable.

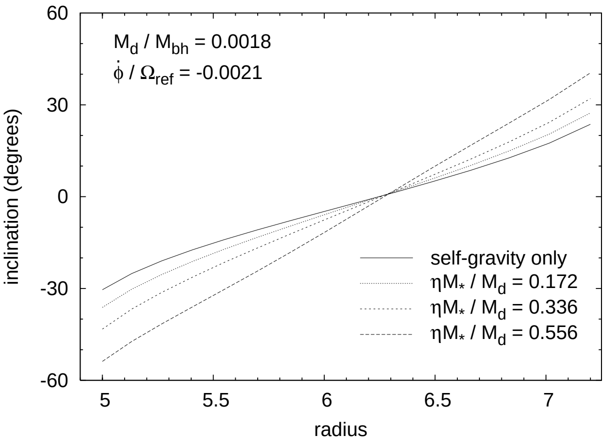

Figure 21. Inclination of a disk of constant surface density at different radii, under the self-gravity torques and the quadrupole torques of a surrounding star cluster. This is parametrized by the ratio $\eta M_*/M_d$, where η measures the flattening of the potential (equation (2) of Sparke 1986) and M_*/M_d is the ratio of the mass of the star cluster to the mass of the disk, inside the outermost ring radius.

In constructing these solutions, we have neglected the background potential generated by the surrounding nuclear star cluster, whose quadruple moment will often be important on scales of ∼ 0.1 pc. Figure 21 shows steadily precessing warped disk inclinations for one case including the background potential. For the parameters chosen, the solutions are qualitatively similar to those discussed earlier.

Stability was tested with respect to perturbations of the ring parameters, that is, the orbits of gas and stars were assumed to remain circular. We did not investigate instabilities by which the disk would become eccentric or lop-sided. Answering the question whether such instabilities are relevant for the warped disks considered here requires different techniques and must remain for future work (see, e.g., Touma 2002).

Neglecting gas pressure and viscosity for our warped disk solutions is justified if the disks are cold and the viscous time-scale is much longer than the precession time-scale. Pringle (1992) has devised a system of equations for the evolution of the surface density and local angular momentum vector of a non-linearly warped, viscous disk. A logical next step is to add the gravitational torques to these equations and study the evolution of viscous, self-gravitating, non-linearly warped disks; this is work in progress.

4.2 Origin of Warped Disks

An important question is whether, and if so how, the warped nuclear disks we have considered can be set up in nature. Infall of gas clouds on inclined orbits has been discussed in the context of observations of the Galactic center (see next section) as a possible model for generating a warped disk in the central parsec (Hobbs & Nayakshin 2009). If the potential of the nuclear star cluster is important, accretion of gas onto a plane inclined relative to its principal plane may lead to a warped disk. The combined quadrupole moment of the gas disk itself and of the background cluster potential would cause the orbits to precess and the disk to become warped. In both cases, the accreting gaseous material with misaligned angular momenta will not directly end up in a warped disk with the right density structure for steady state precession. However, the disk may settle into a warp mode if the energy associated with the transient response can be transported outwards by bending waves (Toomre 1983; Hofner & Sparke 1994), or in the case of gaseous disks, if it can be dissipated (see discussion in Papaloizou et al. 1998); this remains to be investigated.

Caproni et al. (2006) discuss four warping mechanisms for extragalactic accretion disks: tidal, irradiative, magnetic, and Bardeen-Petterson. If a planar disk has become warped by the radiation pressure instability discussed by Petterson (1977); Pringle (1996) or through magnetic instabilities (Lai 2003), the gravitational torques might start to dominate once the source of the initial warping disappears. Highly warped disks have been reported before by Pringle (1997) in the context of the radiation pressure instability. We have done some simple time evolution calculations to show that initially highly warped disks often do not dissolve through self-gravity precession; the torques then cause wobbling but not break-up of the disk. The role of self-gravity in such models would be to ensure the long term persistence of the warp. Future work along the lines discussed at the end of the last subsection may be able to clarify whether this is feasible.

4.3 Warped Disks in Galactic Nuclei

Warped disks around central black holes have been inferred through observations of water maser emission in several nearby active galaxies such as NGC 4258, NGC 1068, and the Circinus galaxy. The maser disks in these galaxies extend radially between $0.16-0.28$ pc (Herrnstein et al. 1999), $0.65-0.11$ pc (Greenhill & Gwinn 1997), and $0.11-0.4$ pc (Greenhill et al. 2003b), respectively. The most widely studied of these maser disks is in NGC 4258, where from the near-Keplerian rotation curve of the high-velocity masers the black hole mass is deduced to be $3.8 \times 10^7 M_\odot$, and the dynamical upper limit to the mass of the disk is $< 10^6 M_\odot$ (Herrnstein et al. 2005). Stationary, power-law accretion disk models constrained by theory and observations have mass fractions $10^{-4} - 10^{-3}$ of the central black hole, in which case the gravitational and viscous torques are comparable (Caproni et al. 2007; Martin 2008). Several explanations have been suggested for the observed warp in the disk (Caproni et al. 2006). In one model the warp is caused by a binary companion orbiting outside the disk (Papaloizou et al. 1998); this would need a mass comparable to that of the disk. A second possibility is radiation pressure from the central source (Pringle 1996; Maloney et al. 1996), but Caproni et al. (2006) analysing several AGN disks find that these are stable against radiation warping. The most favoured explanation for the warp is the Bardeen-Petterson effect (Caproni et al. 2007; Martin 2008) but to reach a steady state the disk must be very long-lived. Gravitational torques have so far been mostly neglected; our results suggest that it may be worthwhile to consider models including both the gravity from the disk and possibly the quadrupole moment of the stellar cusp.

In the Galactic center, near-infrared observations have identified one or possibly two disks of young stars at a distance of ~ 0.04 to 0.4 pc from the central black hole SgrA* (Genzel et al. 2003; Paumard et al. 2006; Lu et al. 2009; Bartko et al. 2009). These stellar disks are highly inclined both with respect to the Galactic plane, and with respect to each other. The total mass in the disks, as inferred from stellar number counts, is around 10^4 $\mathrm{M}_\odot$ (Paumard et al. 2006). This is a non-negligible fraction of the mass of SgrA*, $M_{\mathrm{bh}} \sim 4 \times 10^6$ $\mathrm{M}_\odot$ (Genzel et al. 2000; Ghez et al. 2005). The recent analysis of Bartko et al. (2009) shows that the clockwise rotating disk is warped, with angular momentum direction slewing over $\sim 60^\circ$ from the inner to the outer stars. We consider the precession of the warped disk in the Galactic center elsewhere.

Warped disks could also have important implications for the unification of AGN (Phinney 1989). The unification theories rely on the obscuration along some lines-of-sight of the radiation from the central source by intervening matter. While this obscuring matter is usually depicted as a doughnut-like torus, an alternative possibility is that it could have the shape of a flared or warped disk. The highly warped solutions discussed above in principle provide the geometry to obscure the central engine from most lines-of-sight. The obscuring medium required for these unification scenarios must be clumpy (Nenkova et al. 2002), perhaps suggesting fragmentation of the disk (Goodman 2003). Nayakshin (2005) studied the evolution of a highly inclined warped disk, where he showed that the disk indeed can conceal the central object for most of its lifetime. In the nonlinear regime, warped disks can obscure a significant part of the solid angle of the source (see Figure 12 in Section 3 above). Recently, Wu et al. (2008) showed that because the outer parts of a warped disk receive a larger fraction of the central emission, the line ratios of the reprocessed Balmer emission lines can be successfully predicted by a warped disk model.

5 SUMMARY AND CONCLUSIONS

In this paper we have investigated non-linearly warped disk solutions around black holes for which the only acting force is gravity. We used a simple model in which the disk is approximated as a nested sequence of circular rings. We have shown that with these approximations stable, steadily precessing, highly warped disks can be constructed.

These disks have a common line-of-nodes for all rings. In all cases there is a middle section of the disk which lies approximately in this plane, whereas the inner and outer parts warp away from this plane in opposite directions. The warp angles of these solutions can be very large, up to $\sim \pm 120$ deg, but they extend only over a limited radial range, such that the typical ratio of the outer to the inner boundary radius is $\sim$ 2-4. Such precessing equilibria exist for a wide range of disk-to-black hole mass ratios M_d/M_{bh}, including quite massive disks.

The stability of these precessing disks was determined using linear perturbation theory and, in a few cases, confirmed by numerical integration of the equations of motion. We found that over most of the parameter range investigated, the precessing equilibria are stable, but some are unstable.

These disks obey a scaling relation: they can be scaled to arbitrary radii r, provided the precession speed is scaled to the circular frequency $\Omega(r)$, and they can be scaled in mass, provided the ratio of precession frequency to $\Omega(r)$ is changed, in good approximation, proportionally to the ratio of disk mass to black hole mass.

The main result of this study is that persistent forcing of the disk other than by its own self-gravity is not necessarily required for maintaining a non-linearly warped disk in a Keplerian potential. Further work combining self-gravity with gas physics etc. will show whether these self-gravitating warped disk solutions help to understand the observed warped disks in galactic nuclei.

REFERENCES

Arnaboldi, M. & Sparke, L. S. 1994, AJ, 107, 958

Bardeen, J. M. & Petterson, J. A. 1975, ApJ, 195, L65+

Bartko, H., Martins, F., Fritz, T. K., Genzel, R., Levin, Y., Perets, H. B., Paumard, T., Nayakshin, S., Gerhard, O., Alexander, T., Dodds-Eden, K., Eisenhauer, F., Gillessen, S., Mascetti, L., Ott, T., Perrin, G., Pfuhl, O., Reid, M. J., Rouan, D., Sternberg, A., & Trippe, S. 2009, ApJ, 697, 1741

Binney, J., Jiang, I.-G., & Dutta, S. 1998, MNRAS, 297, 1237

Binney, J. & Tremaine, S. 1987, Galactic dynamics (Princeton, NJ, Princeton University Press, 1987, 747 p.)

Caproni, A., Abraham, Z., Livio, M., & Mosquera Cuesta, H. J. 2007, MNRAS, 379, 135

Caproni, A., Livio, M., Abraham, Z., & Mosquera Cuesta, H. J. 2006, ApJ, 653, 112

Gallimore, J. F., Baum, S. A., & O'Dea, C. P. 2004, ApJ, 613, 794

Genzel, R., Pichon, C., Eckart, A., Gerhard, O. E., & Ott, T. 2000, MNRAS, 317, 348

Genzel, R., Schödel, R., Ott, T., Eisenhauer, F., Hofmann, R., Lehnert, M., Eckart, A., Alexander, T., Sternberg, A., Lenzen, R., Clénet, Y., Lacombe, F., Rouan, D., Renzini, A., & Tacconi-Garman, L. E. 2003, ApJ, 594, 812

Ghez, A. M., Salim, S., Hornstein, S. D., Tanner, A., Lu, J. R., Morris, M., Becklin, E. E., & Duchêne, G. 2005, ApJ, 620, 744

Goldreich, P. 1966, Reviews of Geophysics, 4, 411

Goldstein, H., Poole, C., & Safko, J. 2002, Classical mechanics (Classical mechanics (3rd ed.) by H. Goldstein, C. Poolo, and J. Safko. San Francisco: Addison-Wesley, 2002.)
Goodman, J. 2003, MNRAS, 339, 937
Greenhill, L. J., Booth, R. S., Ellingsen, S. P., Herrnstein, J. R., Jauncey, D. L., McCulloch, P. M., Moran, J. M., Norris, R. P., Reynolds, J. E., & Tzioumis, A. K. 2003a, ApJ, 590, 162
—. 2003b, ApJ, 590, 162
Greenhill, L. J. & Gwinn, C. R. 1997, Ap&SS, 248, 261
Herrnstein, J. R., Greenhill, L. J., & Moran, J. M. 1996, ApJ, 468, L17+
Herrnstein, J. R., Moran, J. M., Greenhill, L. J., Diamond, P. J., Inoue, M., Nakai, N., Miyoshi, M., Henkel, C., & Riess, A. 1999, Nature, 400, 539
Herrnstein, J. R., Moran, J. M., Greenhill, L. J., & Trotter, A. S. 2005, ApJ, 629, 719
Hobbs, A. & Nayakshin, S. 2009, MNRAS, 394, 191
Hofner, P. & Sparke, L. S. 1994, ApJ, 428, 466
Hunter, C. & Toomre, A. 1969, ApJ, 155, 747
Jiang, I.-G. & Binney, J. 1999, MNRAS, 303, L7
Kuijken, K. 1991, ApJ, 376, 467
Lai, D. 2003, ApJ, 591, L119
Lense, J. & Thirring, H. 1918, Physikalische Zeitschrift, 19, 156
Lu, J. R., Ghez, A. M., Hornstein, S. D., Morris, M. R., Becklin, E. E., & Matthews, K. 2009, ApJ, 690, 1463
Maloney, P. R., Begelman, M. C., & Pringle, J. E. 1996, ApJ, 472, 582
Martin, R. G. 2008, MNRAS, 387, 830
Miyoshi, M., Moran, J., Herrnstein, J., Greenhill, L., Nakai, N., Diamond, P., & Inoue, M. 1995, Nature, 373, 127
Natarajan, P. & Armitage, P. J. 1999, MNRAS, 309, 961
Nayakshin, S. 2005, MNRAS, 359, 545
Nelson, R. W. & Tremaine, S. 1995, MNRAS, 275, 897
Nenkova, M., Ivezić, Ž., & Elitzur, M. 2002, ApJ, 570, L9
Papaloizou, J. C. B., Terquem, C., & Lin, D. N. C. 1998, ApJ, 497, 212
Paumard, T., Genzel, R., Martins, F., Nayakshin, S., Beloborodov, A. M., Levin, Y., Trippe, S., Eisenhauer, F., Ott, T., Gillessen, S., Abuter, R., Cuadra, J., Alexander, T., & Sternberg, A. 2006, ApJ, 643, 1011
Petterson, J. A. 1977, ApJ, 216, 827
Phinney, E. S. 1989, in NATO ASIC Proc. 290: Theory of Accretion Disks, ed. F. Meyer, 457–+
Pringle, J. E. 1992, MNRAS, 258, 811
—. 1996, MNRAS, 281, 357
—. 1997, MNRAS, 292, 136
Sparke, L. S. 1984, ApJ, 280, 117
—. 1986, MNRAS, 219, 657
Sparke, L. S. & Casertano, S. 1988, MNRAS, 234, 873
Toomre, A. 1983, in IAU Symposium, Vol. 100, Internal Kinematics and Dynamics of Galaxies, ed. E. Athanassoula, 177–185
Touma, J. R. 2002, MNRAS, 333, 583
Wu, S.-M., Wang, T.-G., & Dong, X.-B. 2008, ArXiv e-prints, 807